CHAPTER IV
RESULTS AND DISCUSSION

4.1 Characterization of TNTs

SEM images of doped and undoped TNTs by hydrothermal treatment are shown in Figure 4.1. As seen in the SEM images, TNTs have tubular and uniform morphology with an average diameter of 2–5 nm and narrow size distribution. Maximum doping of Fe (2%) and Cr (15%) onto TNTs in Figures 4.1b and c, respectively, also showed tubular and uniform morphology, as well.

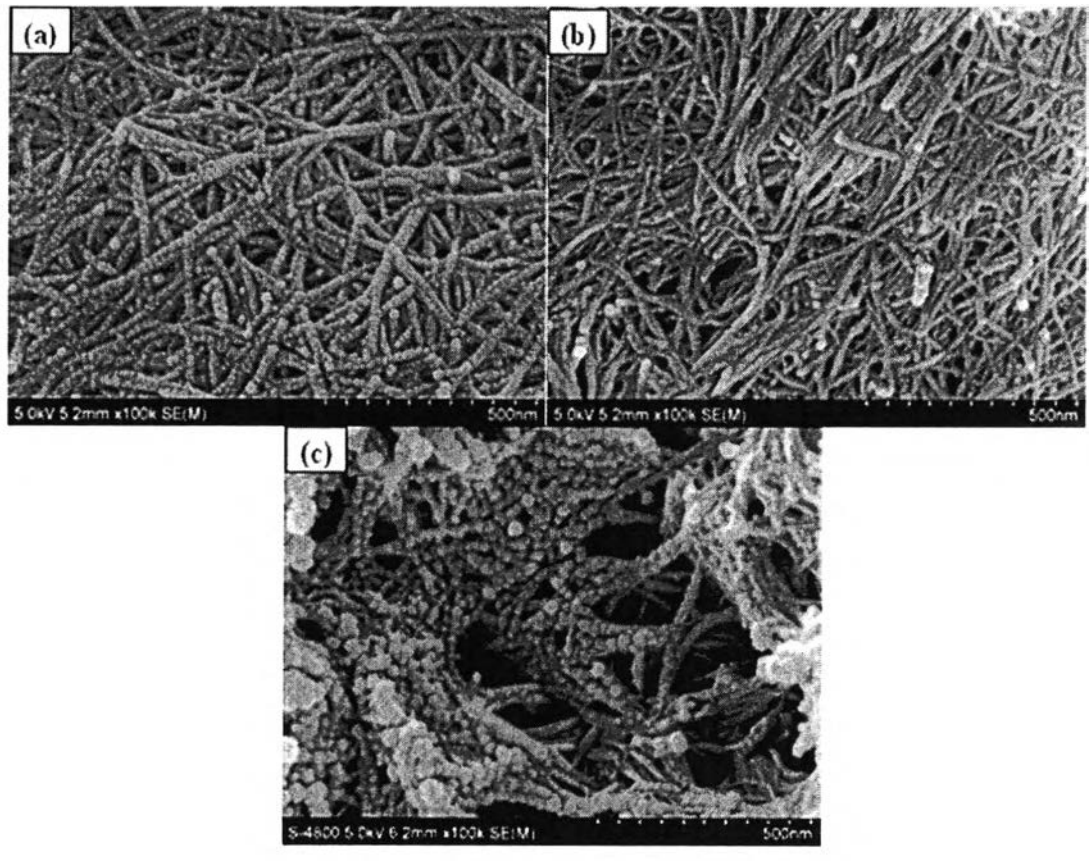

Figure 4.1 SEM images of (a) undoped TNTs, (b) 2% Fe-doped TNTs, and (c) 15% Cr-doped TNTs.

To confirm further, TEM analysis was carried out, as shown in Figure 4.2. Not only undoped TNTs, but also 2% Fe-doped TNTs and 15% Cr-doped TNTs clearly gave nanotubular structures. Figures 4.2a, b and c indicate that the obtained nanotubes were hollow and open-ended. Their diameters were nearly uniform with outer diameter of about 10 nm and more than hundreds of nanometers length, similar to the results reported by previous work (Kasuga *et al.*, 1999). Figures 4.2d, e and f show the TEM images of TNTs, 2% Fe-doped TNTs, and 15% Cr-doped TNTs, respectively, calcined at 500 °C for 2 h. They can be seen that most of the nanotubes still kept their tubular texture after the calcination process.

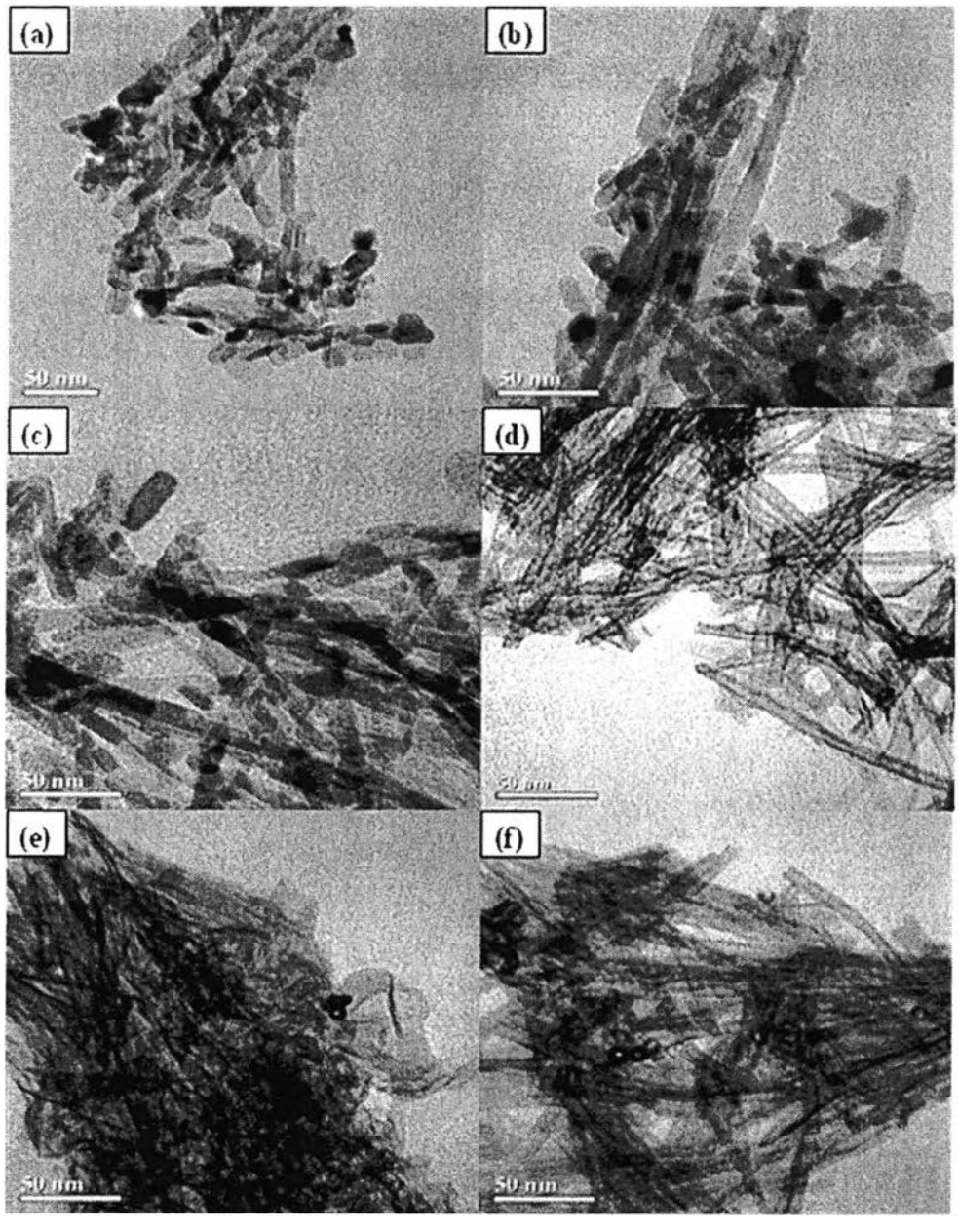

Figure 4.2 TEM images of TNTs, 2% Fe-doped TNTs, and 15% Cr-doped TNTs without (a, b, c) and with calcination at 500 °C for 2 h (d, e, f).

XRD patterns also indicate phase transformation of 2% Fe-doped TNTs without and with calcinations at different temperatures (Figure 4.3). The XRD patterns of Fe-doped TNTs exhibit strong diffraction peaks at 2θ of 25.6°, 38.3°, 47.8°, and 64.2° (Hussain *et al.*, 2011). After calcination at 500 °C, only anatase phase was formed with higher peak intensities, indicating improvement of

crystallinity in some degree. The width of all reflection lines was decreased with increasing calcinations temperatures without a change in the overall patterns of diffraction lines, which is attributed to the enhancement of crysllinity with increasing calcination temperatures.

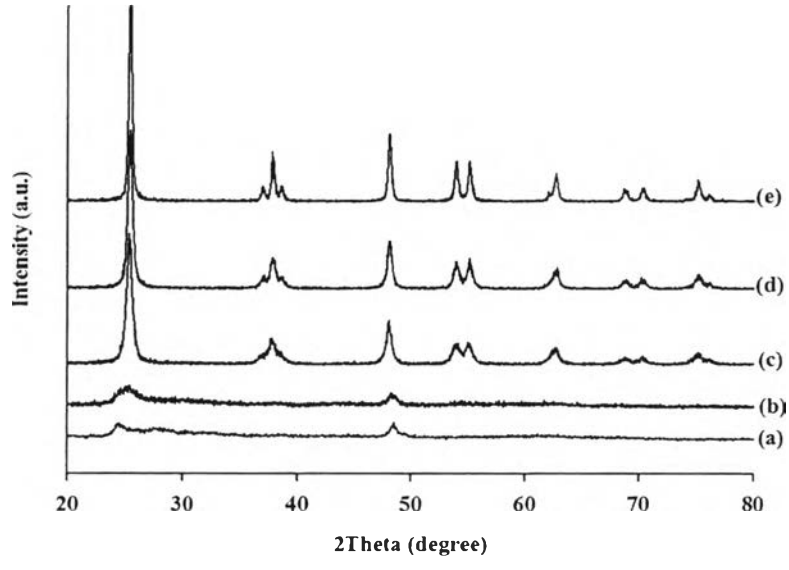

Figure 4.3 XRD patterns of 2% Fe-doped TNTs without (a), and with calcinations at 300 ° (b); 500 ° (c); 600 ° (d); and 700 °C (e) for 2 h.

The XRD patterns of 15% Cr-doped TNTs without and with calcinations at different temperatures in Figure 4.4 show the distinctive peaks at 2θ = 25.3°, 37.8°, 47.7°, 54.0° and 62.4°, corresponding to the anatase crystal planes. These peaks are also observed in all samples, indicating that after TiO_2 modification by doping Cr^{3+} ions, the crystalline structure of the anatase phase still remained (Vu *et al.*, 2010). Notably, after calcination at 500 °C, the anatase peak intensity increased with increasing calcination temperatures, indicating that more crystallization occurred.

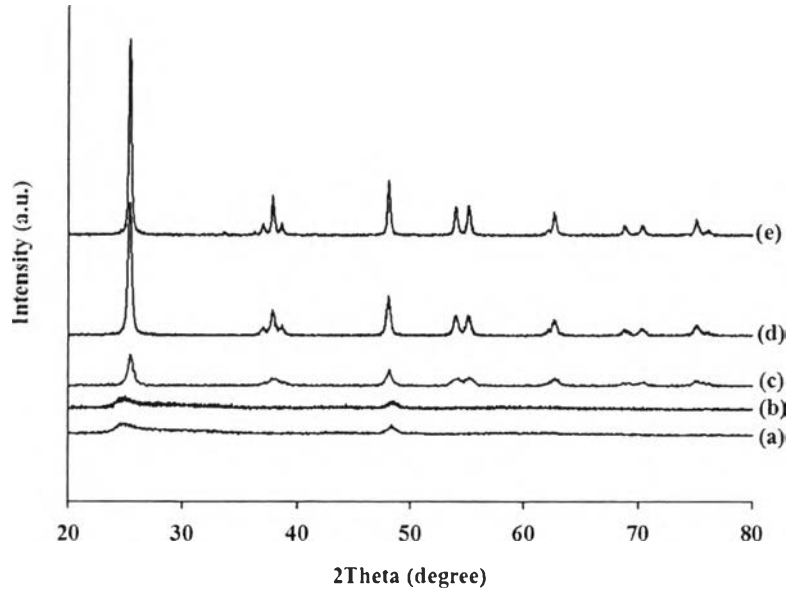

Figure 4.4 XRD patterns of 15% Cr-doped TNTs without (a), and with calcinations at 300 ° (b); 500 ° (c); 600 ° (d); and 700 °C (e) for 2 h.

Figure 4.5 shows the XRD patterns of Fe-doped TNTs calcined at 500 °C with various Fe doping content. All samples only consisted of pure anatase, no indication of rutile or iron oxide phase was observed, even at the highest Fe content, implying that the iron ions were highly dispersed on TiO_2 and the geometry of the synthesized materials was modified without any change in its phase and structure. Comparing to TNTs, the pattern peaks for Fe/TNTs were slightly weaken and broaden. Since the radius of Fe^{3+} is 0.64 °A, which close to the radius of Ti^{4+} (0.68 °A), it could be that Fe^{3+} substitutes Ti^{4+} in the TiO_2 lattice (Deng *et al.*, 2009).

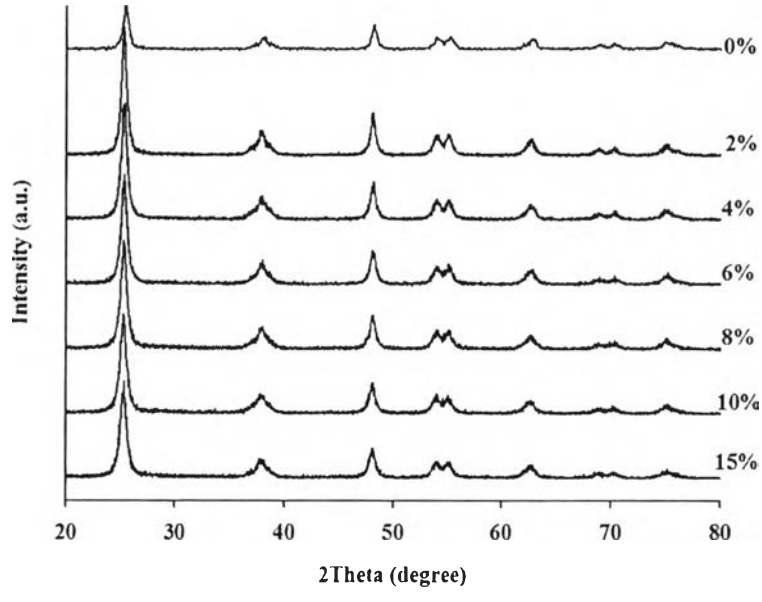

Figure 4.5 XRD patterns of Fe/TNTs calcined at 500 °C for 2 h with various Fe doping contents.

Various Cr doping contents were also studied, as can be seen in Figure 4.6 showing the XRD patterns of Cr-doped TNTs calcined at 500 °C. Only the anatase phase of TiO_2 was formed with no chromium oxide impurity phase detected, even at the highest Cr concent (Zhu *et al.*, 2006) although the diffraction pattern peaks for Cr doped TNTs slightly weaken and broaden, as compared to the pure TNTs. This is not surprising since both the sizes of Cr^{3+} (0.64 ˚A) and Ti^{4+} (0.68 ˚A) ions are very close, making Cr^{3+} ions easily incorporate into the TiO_2 lattice via displacing Ti^{4+} sites (Fan *et al.*, 2008).

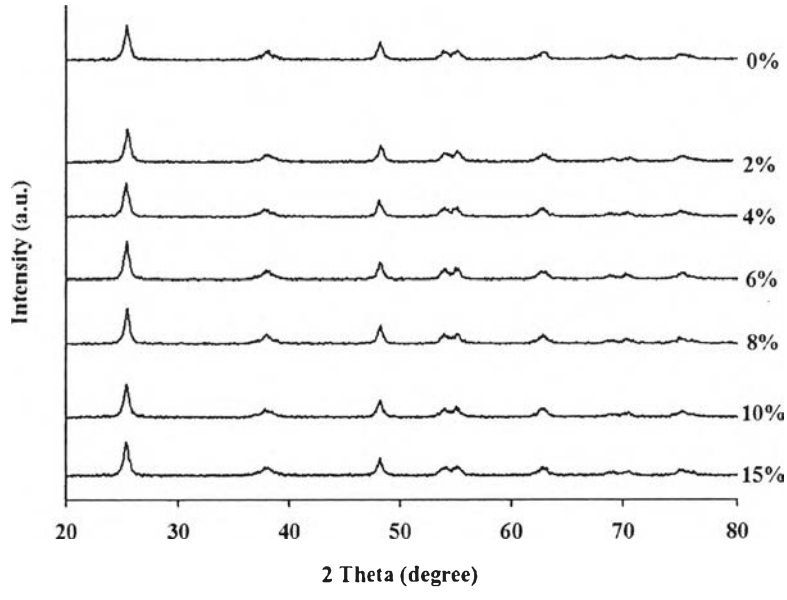

Figure 4.6 XRD patterns of Cr/TNTs calcined at 500 °C for 2 h with various Cr doping contents.

Moreover, the chemical composition and respective percentage of each element present in the samples were analyzed by XRF, as summarized in Table 4.1, presenting the percentages of O, Ti, Na, Cl, Fe, and Cr elements; and confirming the formation of doped TNTs. As seen from Table 4.1, the percentages of metals were found less than actual adding, probably due to not enough time for metal to incorporate with TNTs.

Table 4.1 XRF analysis of M-doped TNTs

Materials	O (%)	Ti (%)	Na (%)	Cl (%)	Fe (%)	Cr (%)
Undoped TNTs	40.02	59.94	-	0.02	-	-
2% Fe-doped TNTs	39.89	59.35	-	0.02	0.72	-
4% Fe-doped TNTs	39.84	58.90	-	0.02	1.24	-
6% Fe-doped TNTs	39.81	58.48	-	0.02	1.69	-
8% Fe-doped TNTs	38.94	58.69	-	0.02	2.35	-
10% Fe-doped TNTs	39.65	57.48	-	0.02	2.85	-
15% Fe-doped TNTs	39.47	56.44	-	0.02	4.07	-
2% Cr-doped TNTs	39.84	58.90	-	0.02	-	1.24
4% Cr-doped TNTs	39.85	58.81	-	0.02	-	1.32
6% Cr-doped TNTs	39.84	58.68	-	0.03	-	1.45
8% Cr-doped TNTs	39.79	58.35	-	0.02	-	1.83
10% Cr-doped TNTs	39.80	58.28	-	0.02	-	1.90
15% Cr-doped TNTs	38.69	59.17	-	0.03	-	2.11

DR-UV was used to confirm whether the metal doped was in framework. Figures 4.7 and 4.8 shows the UV-visible spectra of the samples prepared by adding various contents of Fe and Cr, respectively. The absorption edge of the Fe-doped TNTs displays an obvious shift to the visible light region, as compared to undoped TNTs. This phenomenon may be attributed that Fe doping onto TNTs formed dopant energy level into the band gap of TNTs (Tu *et al.*, 2010). A dopant energy level of Fe was found to be located close to and above the valence band, resulting in a decrease in band gap energy (Asahi *et al.*, 2001). Therefore, the red shift of the absorption edge for the Fe-doped TNTs should come from the electronic transition of the dopant energy level to the conduction band of TNTs. This increase in content of dopant ion

not only shifts the absorption edge towards the visible region, but also increases the absorption of TNTs in the whole visible range (longer wavelength 400–800 nm), causing the shift. The red shift in the visible range is of practical importance since an efficient utilization of visible light for photocatalytic reaction could be possible.

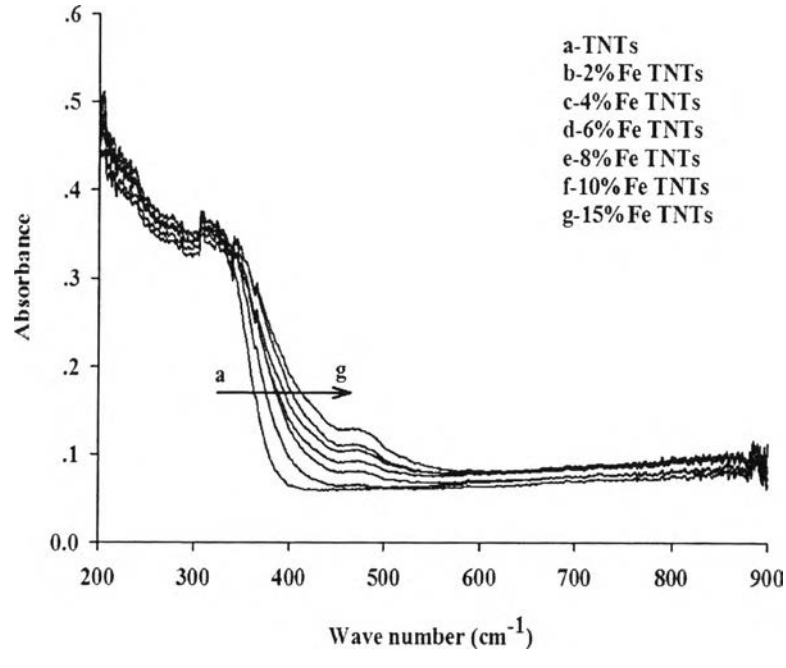

Figure 4.7 UV-visible absorption spectra of TNTs and Fe-doped TNTs.

In case of Cr-doped TNTs, it can be seen that the new absorption appears at 400 to 800 nm in Cr/TNTs, which should be attributed to the Cr doping. The Cr doping induces the shift of the absorption edge to the visible light range and the narrowing of the band gap (Zhang *et al.*, 2008). The narrower band gap value should be due to the introduction to the dope levels, which would induce the excitation of an electron from the valence band to the dope levels. Furthermore, the absorption spectra of the Cr/TNTs reveal more absorption than TNTs from 400 to 800 nm, which indicates the existence of surface states (Wang *et al.*, 2005).

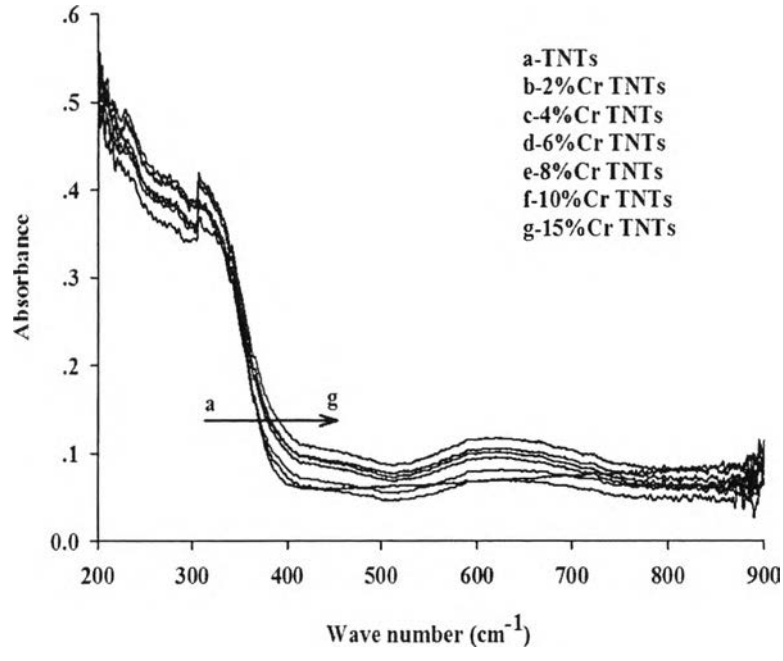

Figure 4.8 UV-visible absorption spectra of TNTs and Cr-doped TNTs.

BET surface area, pore volume, and pore size were analyzed using nitrogen adsorption desorption isotherm and are listed in Table 4.2. N_2 adsorption-desorption isotherm of TNTs, Fe-doped TNTs, and Cr-doped TNTs (Figure 4.9) were classified as a type IV isotherm with H3 hysteresis loop according to IUPAC classification, corresponding to mesopores materials. The surface area of TNTs was impressively obtained, 366.8 m^2/g. As can be seen from the table, the surface area, the pore volume, and the pore diameter increased with increasing metal doping content. Annealing temperature dependency of the specific surface areas for the pure TNTs and the metal doped TNTs are summarized in Table 4.2. High surface area was maintained up to around 300 °C and sudden decrease occurred above the temperature before reaching the value of approximate 110 m^2/g at an annealing temperature higher than 500 °C. From TEM investigation for the annealed TNTs and metal doped TNTs (see Figure 4.2), the samples maintained the nanotubular structure around 500 °C. These facts imply that the as-synthesized TNTs and the metal doped TNTs not only contain some amounts of hydroxyl group (-OH) and/or water (H_2O), but also have TiO_6 octrahedral network structure similar to common anatase-type structure of

TiO_2 crystal. By the heat treatment (annealing) for the as-synthesized TNTs and the metal doped TNTs, H_2O is released and then the sample becomes TiO_2 nanotube with the anatase structure at around 500 °C (Sekino *et al.*, 2010).

Table 4.2 Specific surface area, pore volume, and pore diameter of TNTs and metal-doped TNTs

Sample	Non-calcination			Sample	Calcination		
	Surface area (m^2/g)	Pore volume (ml/g)	Pore diameter (nm)		Surface area (m^2/g)	Pore volume (ml/g)	Pore diameter (nm)
TNT	366.8	0.9697	10.57	**TNT-500**	112.0	0.6733	24.05
2%Fe/TNTs	370.5	0.8526	9.204	**2% Fe/TNTs-300**	337.5	0.9645	11.43
4%Fe/TNTs	389.5	0.9262	9.512	**2% Fe/TNTs-500**	110.7	0.6040	21.82
6%Fe/TNTs	406.5	0.9639	9.485	**2% Fe/TNTs-600**	83.59	0.5426	25.96
8%Fe/TNTs	392.5	0.9216	9.392	**2% Fe/TNTs-700**	41.86	0.2830	27.04
10%Fe/TNTs	358.1	0.8341	9.318	**15% Cr/TNTs-300**	383.8	1.0160	10.59
15%Fe/TNTs	351.7	0.8667	9.856	**15% Cr/TNTs-500**	110.9	0.6385	23.03
2%Cr/TNTs	387.2	0.8918	9.213	**15% Cr/TNTs-600**	64.26	0.4662	29.02
4%Cr/TNTs	372.3	0.8868	9.527	**15% Cr/TNTs-700**	39.05	0.2309	23.65
6%Cr/TNTs	377.8	0.9082	9.615				
8%Cr/TNTs	363.1	0.8762	9.653				
10%Cr/TNTs	392.5	0.9030	9.202				
15%Cr/TNTs	379.1	0.8258	8.715				

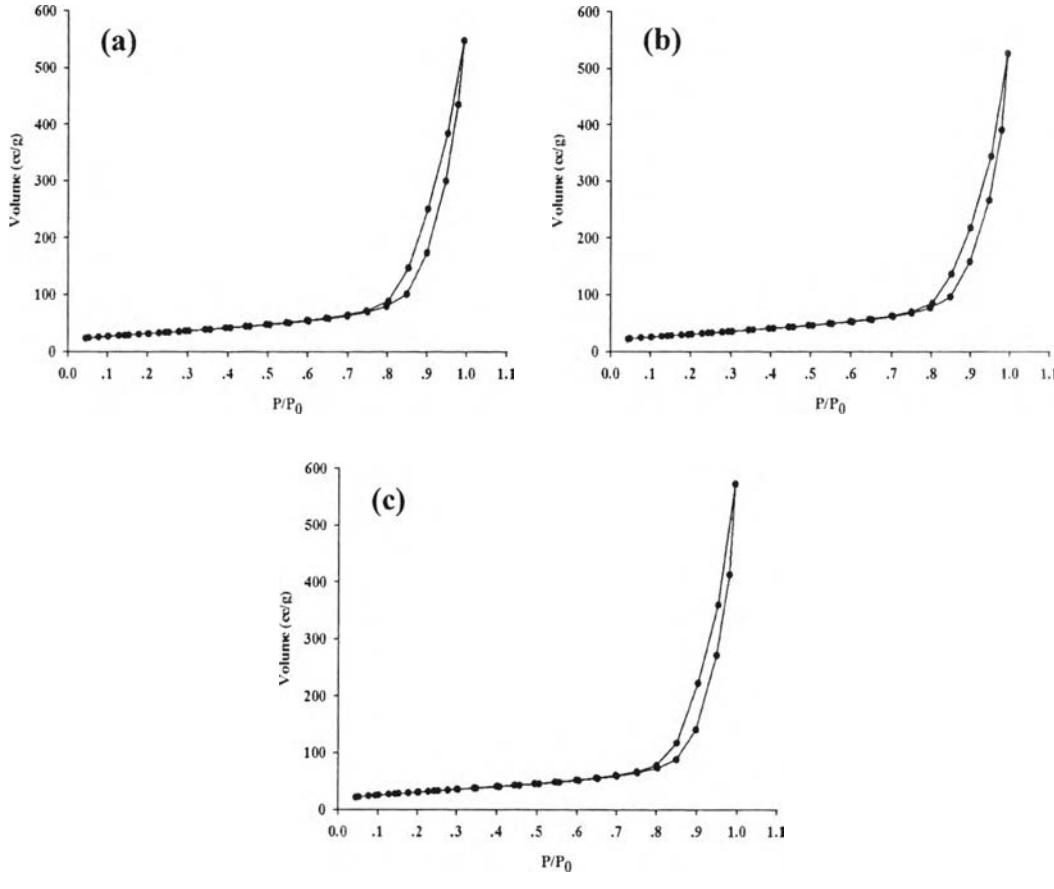

Figure 4.9 The N_2 adsorption-desorption isotherms of TNTs (a), Fe-doped TNTs (b), and Cr-doped TNTs (c) calcined at 500 °C.

4.2 Photocatalytic Activity

4.2.1 Effect of Fe-Doped TNTs

Photochemical breakdown of the chromophoric group (-N=N-) present in the MO molecule for Fe/TNTs as a function of Fe doping content is monitored by UV-vis spectrophotometer. All catalysts were calcined at 500 °C for 2 h. Figure 4.10 shows plots of the MO concentration as a function of irradiation time for different samples. It can be seen that the photocatalytic activity of Fe–doped TNTs increases with decreasing Fe amount. Interestingly, when compared to the pure TNTs, the optimum dopant amount of Fe found to be at 2% was unnoticeably different in photocatalytic activity. This may be due to the fact that a small amount of

Fe^{3+} ions can act as photo-generated holes (h^+) and electron (e^-) traps, and cause the h^+- e^- recombination. Thus, when higher amount of Fe^{3+} dopants was added, it was found that recombination of sites was dominant and resulted in a decrease of the photocatalytic efficiency (Choi *et al.*, 1994). Therefore, it is reasonable that the photocatalytic activities of Fe^{3+}-doped TNTs were decreased accordingly with the further higher doping content.

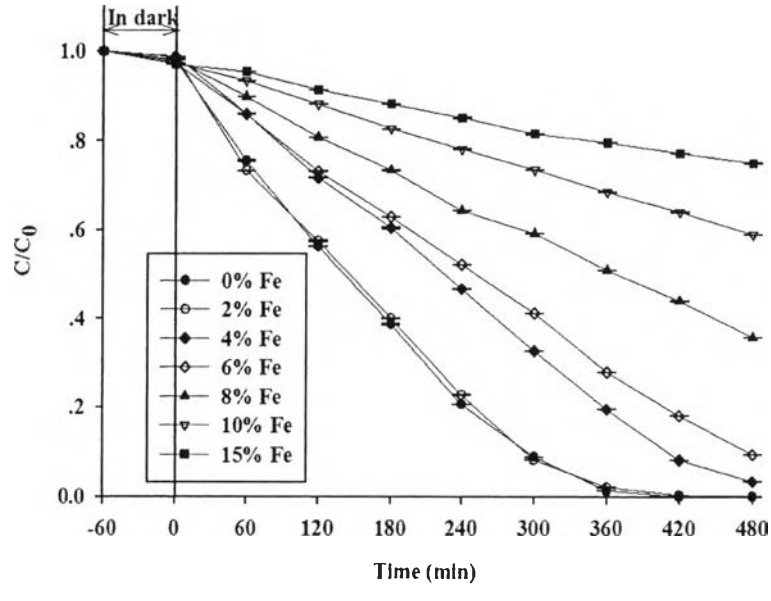

Figure 4.10 Effect of the Fe doping content on the photodegradation of methyl orange after the catalyst was calcined at 500 °C for 2 h.

A possible schematic mechanism diagram of the Fe contributed to the higher activity is described by Li *et al.* in 2009, see Figure 4.11. Generally, TiO_2, having 3.2 eV binding energy, cannot effectively produce enough photo-induced electrons and holes under the visible light irradiation. However, when Fe^{3+} doped onto TiO_2 to form Fe–O–Ti bond, the overlap of the d orbital of Fe^{3+} and Ti will decrease the band gap of Fe–TiO_2 from 3.2 eV to less than 3.2 eV. The decreased band gap of the Fe–TiO_2 is more favorable to generate electron and hole pairs than the pure TiO_2 under visible light irradiation. As shown in Figure 4.11, parts of electrons and holes will be trapped by Fe^{3+} to form Fe^{2+} or Fe^{4+}, respectively. Hence,

more photo-induced electrons and holes will have higher chance to transfer to the catalyst's surface and oxidize/reduce the products prior to the recombination. The holes in the valence band are good oxidants and the electrons in the conduction band are excellent reductants, causing these processes to effectively increase the photocatalytic activity.

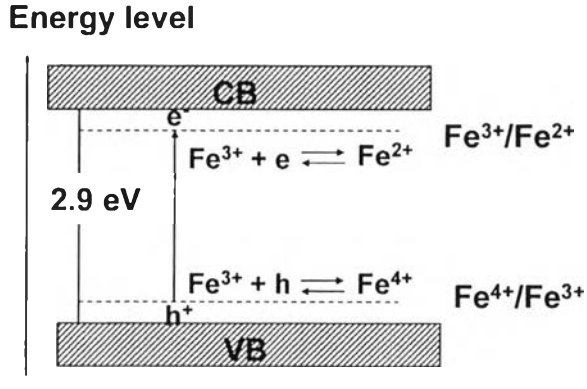

Figure 4.11 Schematic mechanism diagram of the photocatalyic mechanism of Fe-doped TNTs (Li *et al.*, 2009).

4.2.2 Effect of Cr-Doped TNTs

The investigation of visible light activity was continued with Cr-doped TNTs catalyst by the degradation of MO in an aqueous solution. The Cr-doped TNTs calcined at 500 °C for 2 h resulted in the activity shown in Figure 4.12. It was found that the degradation efficiency increased continuously during the process of degradation. Moreover, the Cr-doped TiO_2 provided much higher efficiency than the Fe-doped TNTs for the MO photodegradation, indicating that an appropriate Cr doping could greatly improve the photocatalytic activity of TNTs. This phenomenon can be attributed to the formation of vast oxygen vacancy with Cr doping since Cr-doping introduces substantive oxygen vacancy. The oxygen vacancies in TiO_2 act as electron traps to bind the photo-induced electrons and play a significant role in inhibiting the recombination rate of the photo-induced e^--h^+ pairs. As a result, the process enhances the photocatalytic activity of TNTs (Peng *et al.*, 2012).

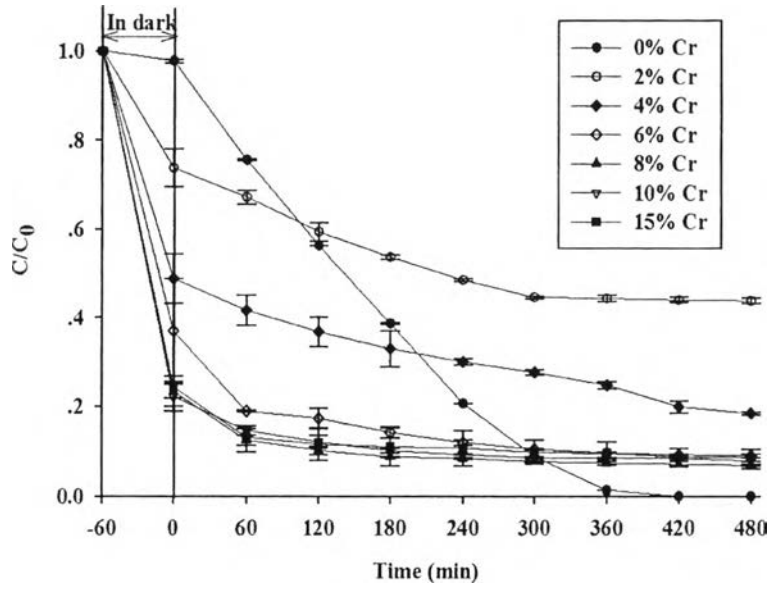

Figure 4.12 Effect of the Cr doping content on the photodegradation of methyl orange after the samples were calcined at 500 °C for 2 h.

Among 500 °C calcined Cr-TNTs, the 15% Cr-TNTs possess the highest photocatalytic activity and was able to decompose MO completely in about 8 h. The anatase phase stability of the nanocrystalline TiO_2 nanotubes with calcinations at 500 °C and also red shift by Cr^{3+} doping are responsible for the highest activity under UV light. As a result of the trivalent Cr doping, a large number of oxygen vacancies are created and these vacancies are the scavengers of the excited electrons. Thus, more recombination of photoexcited e^-/h^+ pairs occurs in the Cr^{3+} doped system. The proposed mechanism of the photocatalysis by Cr^{3+} doping is as follows (Jaimy *et al.*, 2011):

$$Cr^{3+} + h\nu \longrightarrow Cr^{4+} + e^-$$

$$e^- + O_2 \longrightarrow O_2^-$$

$$Cr^{4+} + OH^- \longrightarrow Cr^{3+} + OH^{\bullet}$$

The holes formed can transfer to the surface and active oxygen species, such as hydroxyl and super oxide radicals generated on the surface of the doped TNTs. The photogenerated electrons react with dissolved oxygen to produce superoxide anion radicals and Cr^{4+} ions (holes) react with surface hydroxyl groups to produce hydroxyl radicals, resulting in further photocatalytic activity (Zhu *et al.*, 2006).

4.2.3 Effect of Calcination Temperature

Various calcinations, an effective treatment method to enhance the photocatalytic activity of M-doped TNTs, were studied and the results are shown in Figures 4.13 and 4.14 using Fe- and Cr-doped TNTs, respectively. The MO degradation results of M-doped TNTs with and without calcination after 8 h irradiation indicate that the doped nanotubes without calcination showed much lower photocatalytic activity due to the amorphous structure of TNTs allowing metal species to stay only on the surface. In addition, it has been generally accepted that anatase TiO_2 works better during the photocatalytic process. After the calcination treatment, the amorphous TNTs became the anatase form, inducing higher photocatalytic activity. From Figures 4.3 and 4.4, they can be seen that the content of the anatase TNTs increased with the increase of the calcination temperature. However, the photocatalytic activity of both Fe/TNTs and Cr/TNTs decreased with a further increase in the calcination temperature, probably due to the agglomeration and sintering damage of TNTs caused by high temperature calcination (Xu *et al.*, 2005).

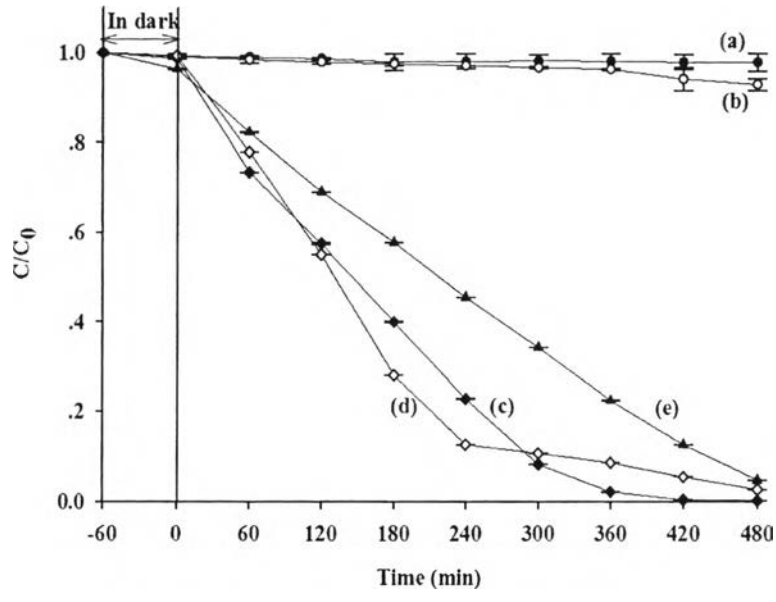

Figure 4.13 Photodegradation of methyl orange by 2% Fe/TNTs without calcination (a) and with calcinations at 300 ° (b); 500 ° (c); 600 ° (d); and 700 °C (e).

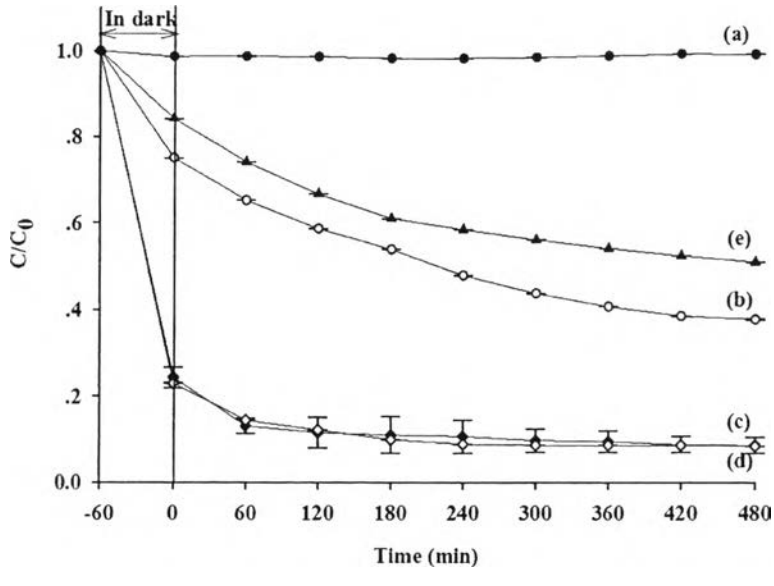

Figure 4.14 Photodegradation of methyl orange by 15% Cr/TNTs without calcination (a) and with calcinations at 300 ° (b); 500 ° (c); 600 ° (d); and 700 °C (e).

4.2.4 Kinetic Analysis

The kinetics of photocatalytic degradation of MO solution was investigated when MO initial concentration was 20 ppm. The linear relationship between $\ln(C_0/C)$ and time in Figure 4.15 demonstrates that the photocatalytic degradation of MO followed pseudo first-order kinetics:

$$\ln C_0/C = kt$$

where C_0 represents initial concentration of the MO dye and C is the concentration of the dye at time t.

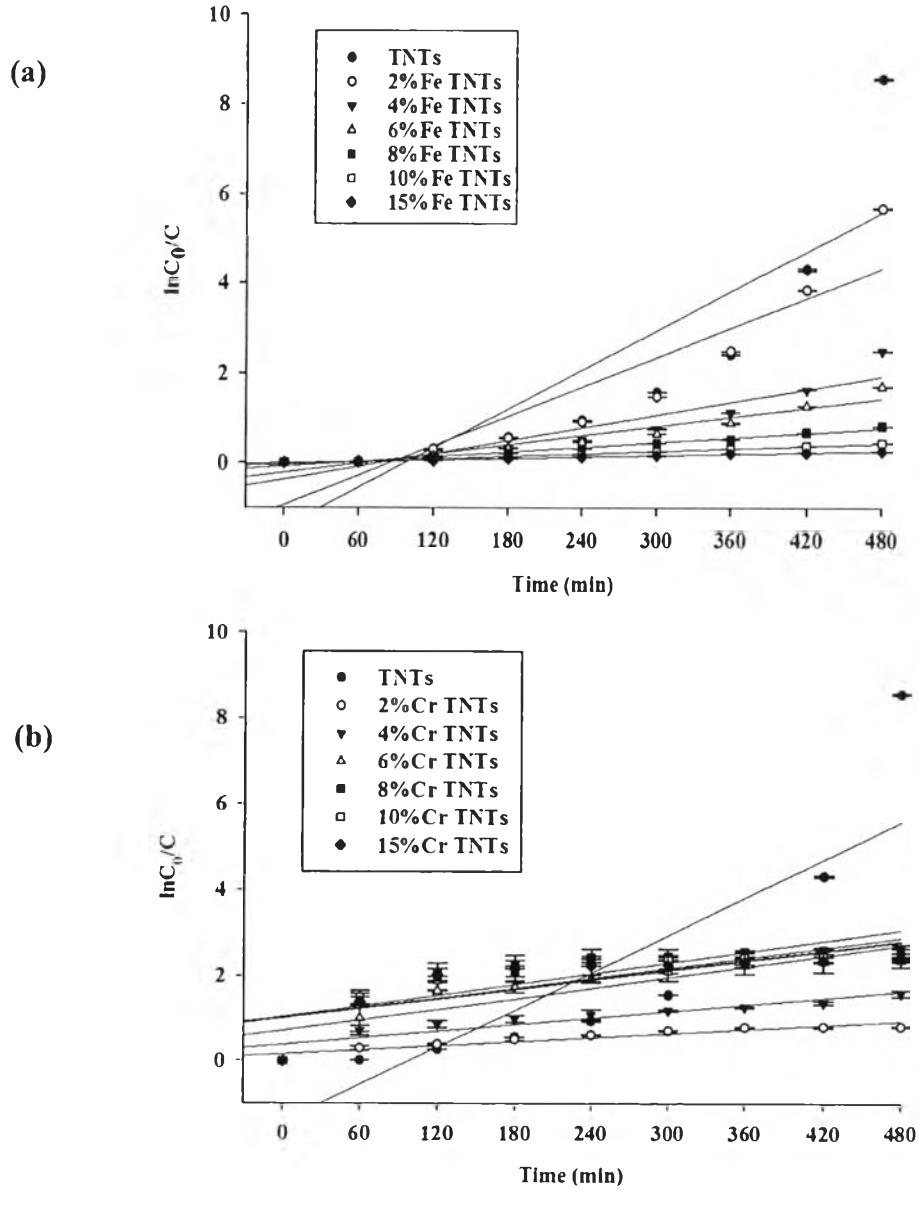

Figure 4.15 Pseudo-first order kinetics for photodegradation of MO on Fe/TNTs (a) and Cr/TNTs (b).

The pseudo-first order kinetic constant was calculated from the slope of the plot between $\ln C_0/C$ and time at each condition. From the plots, the regression coefficient (r) was also obtained (Rashed *et al.*, 2007). Both results obtained in this study are given in Table 4.3. Under the experimental conditions, taking into account the amount of MO present in solution after dark adsorption, it can be assumed that great bulk of the incident photons are absorbed by catalyst, meaning that, in the presence of a heterogeneous photocatalytic process and from the experimental results, it can be explained in terms of two elementary mechanisms: (i) oxidation of the dyestuff through successive attacks by the hydroxyl radical ($HO^{\bullet}$) and (ii) direct reaction of the dyestuff with photogenerated holes in a process similar to the photo-Kolbe reaction (Krauetler *et al.*, 1977). The first process requires that the dyestuff molecules and the other oxygen containing species adsorb in neighbor sites. Oxygen on the TiO_2 surface and in its molecular form acts as electron acceptor, contributing via the superoxide radical ($O_2^{-\bullet}$) to the formation of hydrodioxyl radical ($HO_2^{\bullet}$) which is a known intermediate for the HO• radical. However, the HO• radical should be mainly formed from the adsorbed OH^- and H_2O molecules by electron donation to the photogenerated holes (Li *et al.*, 2006). Together with other highly oxidant species (hydrodioxyl radicals) they are reported to be responsible for the heterogeneous TiO_2 photodecomposition of organic substrates as dyes, as can be expressed as follows:

$$TiO_2 + h\nu\,(UV) \longrightarrow TiO_2\,(eCB^- + hVB^+)$$
$$TiO_2\,(hVB^+) + H_2O \longrightarrow TiO_2 + H^+ + OH^-$$
$$TiO_2\,(hVB^+) + OH^- \longrightarrow TiO_2 + OH^{\bullet}$$
$$TiO_2\,(eCB^-) + O_2 \longrightarrow TiO_2 + O_2^{-\bullet}$$
$$O_2^{-\bullet} + H^+ \longrightarrow HO_2^{\bullet}$$
$$Dye + OH^{\bullet} \longrightarrow \text{degradation products}$$

As a result, the resulting HO• radical, being a very strong oxidizing agent, can oxidize most of methyl orange dye to the mineral end-products (Hoffman *et al.*, 1995).

Table 4.3 Pseudo-first order kinetic constants (k) for photodegradation of MO on M-doped TNTs calcined at 500 °C for 2 h

Samples	Rate constant, k ($\times 10^{-3}$ min^{-1})	r
TNTs	14.544	0.7298
2% Fe/TNTs	10.942	0.8490
4% Fe/TNTs	4.786	0.8726
6% Fe/TNTs	3.442	0.9268
8% Fe/TNTs	1.757	0.9811
10% Fe/TNTs	0.955	0.9903
15% Fe/TNTs	0.561	0.9950
2% Cr/TNTs	1.620	0.8943
4% Cr/TNTs	2.634	0.8432
6% Cr/TNTs	4.163	0.7757
8% Cr/TNTs	4.201	0.6465
10% Cr/TNTs	3.899	0.6408
15% Cr/TNTs	3.700	0.5683

From BET results in Table 4.2, when compared to Fe-TNTs and Cr-TNTs, TNTs show the highest specific surface area and pore volume, resulting in the increase of the photocatalytic activity of MO (Yu *et al.*, 2006). Although BET results of both Fe- and Cr-TNTs show slight difference in both surface area and pore volume, the photocatalytic activity of Fe-TNTs was higher than that of Cr-TNTs because the decomposition of methyl orange occurred in dark for 1h and the decomposition rate became constant as increasing reaction time. Moreover, Fe^{3+} ions increased the degradation rate by inducing Fenton reaction to generate more $^{\bullet}OH$ radicals for decomposing organic compounds, as shown in the following equation (San *et al.*, 2002).

$$Fe^{2+} + H_2O_2 + H^+ \rightarrow Fe^{3+} + {}^{\bullet}OH + H_2O$$